J. Fluid Mech. (1982), *vol.* 123, *pp.* 477–501
Printed in Great Britain

Generalized vortex methods for free-surface flow problems

By GREGORY R. BAKER,† DANIEL I. MEIRON AND STEVEN A. ORSZAG
Massachusetts Institute of Technology, Cambridge, MA 02139

(Received 29 September 1981 and in revised form 5 April 1982)

The motion of free surfaces in incompressible, irrotational, inviscid layered flows is studied by evolution equations for the position of the free surfaces and appropriate dipole (vortex) and source strengths. The resulting Fredholm integral equations of the second kind may be solved efficiently in both storage and work by iteration in both two and three dimensions. Applications to breaking water waves over finite-bottom topography and interacting triads of surface and interfacial waves are given.

1. Introduction

It is well known that the solution to the Dirichlet and Neumann problems for Laplace's equation may be expressed in terms of boundary integrals of source or dipole distributions. The equations determining the source and dipole strengths are Fredholm integral equations of the first and second kind, as enumerated in table 1. These equations are normally solved by direct matrix-inversion techniques such as Gaussian elimination. However, when the problems are formulated in terms of integral equations of the second kind, it is not necessary to resort to such costly inversion methods; the required Fredholm equations have globally convergent Neumann series, so they may be solved by simple iterative procedures. These iterative methods lead to new and efficient techniques for the solution of time-dependent, irrotational, incompressible flows in layered media in the presence of both free surfaces and solid bodies.

With N points used to resolve the fluid interfaces (in either two or three space dimensions), our iterative boundary integral methods require only $O(N)$ computer storage and $O(N^2)$ arithmetic operations per time step. These storage and operation counts should be contrasted with more conventional methods based on direct matrix inversion that require $O(N^2)$ storage and $O(N^3)$ work per time step. As problem complexity increases, our new methods offer increasing advantages over more classical approaches (see e.g. Chan & Street 1970; Longuet-Higgins & Cokelet 1976).

Previously we have obtained results by our methods for multifrequency Rayleigh–Taylor instability of semi-infinite (Baker, Meiron & Orszag 1980) and thin (Verdon *et al.* 1982) fluid layers. In the present paper, applications to nonlinear water waves are given as well as a detailed derivation of the governing equations.

In §2 we derive the kinematical and dynamical equations used to evolve free surface flows. In §3 applications to large-amplitude surface and interfacial water waves are given. In §4, the methods are extended to flows over bottom topography and applications to nonlinear waves are given. Then, in §5 the interaction of triads of surface and interfacial waves is studied and the results are compared with the

† Present address: Department of Mathematics, University of Arizona, Tucson.

	Representation	
Problem type	Source	Dipole
Dirichlet	First kind	Second kind
Neumann	Second kind	First kind

TABLE 1. Classification of Fredholm integral equation by problem type and choice of representation

predictions of asymptotic theory. Finally, in §6, some extensions of the present methods are described. A new formulation of the equations describing nonlinear interfacial waves of permanent form is given in the appendix.

2. Equations of motion

In this section, we derive evolution equations for the motion of interfaces between layers of incompressible, inviscid, irrotational fluid. The density is constant in each layer, but may jump in value across an interface. Thus vorticity will in general be created baroclinically at interfaces but not in the interior of the layers. Consequently, the interfaces may be regarded as vortex sheets whose strength changes in time owing to the presence of the density discontinuities. The task at hand is to obtain equations describing the motion of the interface and the production of vorticity at the interface.

Since a vortex sheet is closely related to a surface distribution of dipoles, we may take particular advantage of several important results from classical potential theory (see Kellogg 1953; Bergman & Schiffer 1953). The flow in each layer is incompressible and irrotational, so there is a piecewise smooth velocity potential ϕ satisfying Laplace's equation. Classical potential theory shows that the potential may be written as a boundary integral of dipoles. In particular, this representation implies a continuous normal derivative for the potential at each interface, thus satisfying the kinematical condition of continuous normal velocity. The dipole strength μ is related to the jump in potential across an interface. Since the vortex-sheet strength Γ is the jump in tangential velocity at the interface, there is an obvious relationship between Γ and μ. Specifically, in two dimensions, Γ is related to the arclength derivative of μ. Thus we have a choice of calculating the time evolution of Γ or μ. In specific applications, we shall see that the numerics dictates which one should be used.

The most important result for our purposes from classical potential theory is that the Dirichlet or Neumann problems for Laplace's equation may be expressed as Fredholm integral equations of the second kind and that these equations may be solved iteratively as their Neumann series are globally convergent. We shall also show that the evolution equation for the dipole strength or the vortex-sheet strength is a Fredholm integral equation of the second kind and that it has a convergent Neumann series. These facts allow an efficient numerical procedure for calculating the motion of free surfaces.

In this paper we restrict attention to two-dimensional flows that are periodic in the horizontal coordinate x with period 2π (for a discussion of problems involving radiation boundary conditions see Baker, Meiron & Orszag 1982). The vertical coordinate is denoted by y.

The potential of a dipole layer of strength $\mu(e)$ distributed along the interface

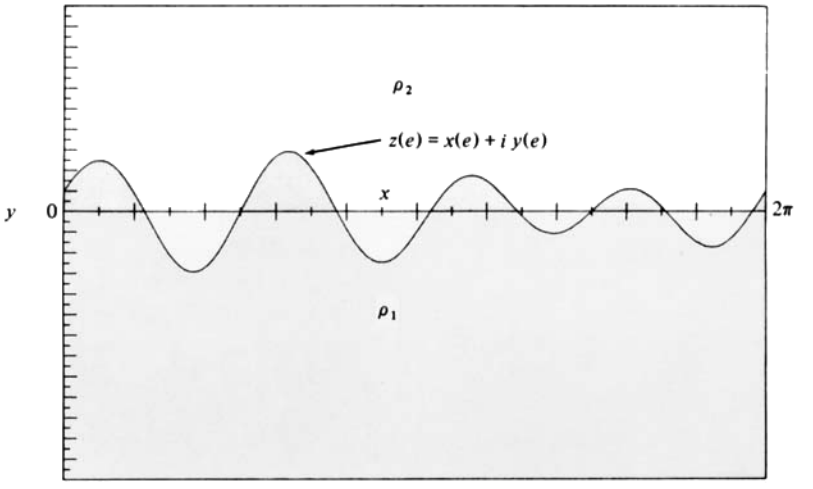

FIGURE 1. Flow geometry for interfacial flow between two fluids of infinite extent.

parametrized by $x(e)$, $y(e)$ is

$$\phi(x,y) = -\int_{-\infty}^{\infty} \mu(e)\frac{\partial G}{\partial \nu} s_e\, de, \tag{2.1}$$

where $G = (4\pi)^{-1}\ln[(x-x(e))^2+(y-y(e))^2]$ is the free-space Green function, ν is the downward normal (see figure 1), and $s_e^2 = x_e^2+y_e^2$. The subscript e denotes differentiation with respect to the label e, which will later be chosen to be a Lagrangian variable. The normal derivative of G in (2.1) is taken with respect to the normal at the integration point labelled by e:

$$\frac{\partial G}{\partial \nu} = \frac{x_e(e)\,(y-y(e)) - y_e(e)\,(x-x(e))}{2\pi s_e[(x-x(e))^2+(y-y(e))^2]}. \tag{2.2}$$

We introduce the notation $z = x+iy$ for the complex field point, $\Phi = \phi+i\psi$ for the complex potential, where ψ is the stream function, and $q = u+iv$ for the complex velocity, where u and v are respectively the x and y velocity components. Then $q^* = d\Phi/dz$, where the asterisk indicates complex conjugation.

Using (2.1), the complex potential may be written as the integral

$$\begin{aligned}\Phi(z) &= \frac{1}{2\pi i}\int_{-\infty}^{\infty} \mu(e)\frac{z_e(e)}{z-z(e)}\,de + \Phi_{\mathrm{E}}(z)\\ &= \frac{1}{4\pi i}\int_0^{2\pi} \mu(e)\, z_e(e)\cot\tfrac{1}{2}[z-z(e)]\,de + \Phi_{\mathrm{E}}(z),\end{aligned} \tag{2.3}$$

where the integrations are to be performed along the interface, which is parametrized as $z(e)$ with $0 \leqslant e < 2\pi$ extended periodically. Note that the range of integration is finite; the contributions to the potential from periodic extensions of the interface has been summed in closed form. The contribution to the potential from the integral (2.3) approaches a constant exponentially fast as $R \to \infty$, where R is a measure of the distance from the interface. (On the other hand, for interfaces that are finite closed curves, $\Phi(z)$ decays like $1/R$ as $R \to \infty$.) In (2.3) Φ_{E} accounts for the presence of any external flow that does not vanish far from the interface.

In general, several interfaces may be present. The potential is then written as a sum of integrals along each interface. However, for simplicity of notation and presentation we consider only one interface in the subsequent derivation of the governing evolution equations. Our results extend immediately to the case of more interfaces, provided that they do not intersect one another.

We shall use subscript 1 (or 2) to refer to quantities of the fluid below (or above) the interface (see figure 1). Recall that the potential is discontinuous across the interface, while the stream function is continuous. Thus the dipole strength, which is the jump in potential across the interface, may be written in terms of the complex potential:

$$\mu(e) = \Phi_1(e) - \Phi_2(e).$$

The average value of the complex potential at the interface,

$$\Phi(e) = \tfrac{1}{2}(\Phi_1(e) + \Phi_2(e)), \tag{2.4}$$

may be calculated by taking the principal value of the integral in (2.3). Consequently the average complex velocity at the interface is

$$q^*(e) = \Phi_e(e)/z_e(e). \tag{2.5}$$

The complex velocity may be expressed directly in terms of a boundary integral by differentiating (2.3) and then integrating by parts:

$$u(z) - iv(z) = \frac{1}{4\pi i}\int_0^{2\pi} \gamma(e) \cot \tfrac{1}{2}[z - z(e)]\, de + Q_{\mathrm{E}}^*(z). \tag{2.6}$$

Here Q_{E} is the external flow corresponding to the potential Φ_{E}, and

$$\gamma(e) = \Gamma(e)\, s_e = \mu_e,$$

where $s_e^2 = z_e^* z_e$. The integral in (2.6) is a form of the Biot–Savart integral in terms of the unnormalized vortex-sheet strength γ. Once again, the velocity at the interface determined by the principal value of the integral is the average of those just above and below the interface.

It is conventional to use the average of the velocities on either side of the sheet as the velocity for the motion of the Lagrangian points describing the vortex sheet. However, this choice is not necessary and is, in some cases, inconvenient. More generally, we define the velocity $\tilde{q}$ of a Lagrangian point, labelled by e, as a weighted average of the velocities across the interface. In this way, we still satisfy the kinematics but retain some control over the positioning of the Lagrangian markers. Thus

$$\frac{\partial z^*}{\partial t}(e,t) \equiv \tilde{q}^*(e) = q^*(e) + \frac{\alpha\gamma}{2z_e}, \tag{2.7}$$

where $|\alpha| \leqslant 1$ is the weighting factor. Note that, by choosing $\alpha = 1$ or -1, the Lagrangian motion follows the lower or upper fluid at the interface. Equation (2.7) is the kinematical evolution equation for the interface.

The evolution equation for the dipole strength or the vortex-sheet strength is derived as follows. First, evaluating Bernoulli's equation on either side of the interface using the Lagrangian time derivative defined by (2.7) gives

$$\frac{\partial \phi_1}{\partial t} - \mathrm{Re}\{\tilde{q}^* q_1\} + \tfrac{1}{2} q_1^* q_1 + \frac{p}{\rho_1} + gy = 0, \tag{2.8}$$

$$\frac{\partial \phi_2}{\partial t} - \mathrm{Re}\{\tilde{q}^* q_2\} + \tfrac{1}{2} q_2^* q_2 + \frac{p}{\rho_2} + gy = 0. \tag{2.9}$$

Here g is the acceleration due to gravity, ρ is the density and p is the pressure, which is assumed to be continuous across the interface. If surface forces such as surface tension are present, the pressure will jump in value by a known amount, which may be easily incorporated into (2.8), (2.9).

From (2.6) it follows that

$$q_1^* = \tilde{q}^* + \frac{(1-\alpha)\gamma}{2z_e}, \tag{2.10}$$

$$q_2^* = \tilde{q}^* - \frac{(1+\alpha)\gamma}{2z_e}. \tag{2.11}$$

Then subtracting (2.8) from (2.9) gives

$$\frac{\partial \mu}{\partial t} - \frac{\alpha\gamma^2}{2z_e^* z_e} + \frac{\rho_2-\rho_1}{\rho_1\rho_2} p = 0. \tag{2.12}$$

Differentiating this equation with respect to e gives a similar equation for γ:

$$\frac{\partial \gamma}{\partial t} - \tfrac{1}{2}\alpha \frac{\partial}{\partial e}\frac{\gamma^2}{z_e^* z_e} + \frac{\rho_2-\rho_1}{\rho_1\rho_2} p_e = 0.$$

Similarly, by adding (2.8) and (2.9), we obtain

$$2\,\mathrm{Re}\left\{\frac{\partial \Phi}{\partial t}\right\} - qq^* - \alpha\gamma\,\mathrm{Re}\left\{\frac{q}{z_e}\right\} + \frac{\gamma^2}{4z_e z_e^*} + \frac{\rho_1+\rho_2}{\rho_1\rho_2} p + 2gy = 0. \tag{2.13}$$

Eliminating p between (2.12) and (2.13) gives

$$\frac{\partial \mu}{\partial t} - \frac{\alpha\gamma^2}{2z_e z_e^*} = -2A\left[\mathrm{Re}\left\{\frac{\partial \Phi}{\partial t}\right\} - \tfrac{1}{2}q^*q - \tfrac{1}{2}\alpha\gamma\,\mathrm{Re}\left\{\frac{q}{z_e}\right\} + \frac{\gamma^2}{8z_e z_e^*} + gy\right]. \tag{2.14}$$

The above equation is the evolution equation for μ as the interface advects. By differentiating (2.14) with respect to e, there results an evolution equation for γ:

$$\frac{\partial \gamma}{\partial t} - \tfrac{1}{2}\alpha \frac{\partial}{\partial e}\frac{\gamma^2}{z_e z_e^*} = -2A\left[\mathrm{Re}\left\{\frac{\partial q^*}{\partial t} z_e\right\} - \tfrac{1}{2}\alpha\gamma\,\mathrm{Re}\left\{\frac{q_e}{z_e}\right\} + \frac{1}{8}\frac{\partial}{\partial e}\frac{\gamma^2}{z_e z_e^*} + g y_e\right]. \tag{2.15}$$

The parameter A in the above two equations is the Atwood ratio, defined as

$$A = \frac{\rho_1-\rho_2}{\rho_1+\rho_2}. \tag{2.16}$$

The quantity $\partial\Phi/\partial t$ in (2.14) is obtained by Lagrangian time differentiation of (2.3). Specifically,

$$\frac{\partial \Phi}{\partial t}(e) = \frac{1}{4\pi i}\mathrm{P}\int_0^{2\pi}\left[\frac{\partial \mu}{\partial t}(e')\, z_e(e') + \mu(e')\,\tilde{q}_e(e')\right]\cot\tfrac{1}{2}[z(e)-z(e')]\,de'$$
$$-\frac{1}{8\pi i}\mathrm{P}\int_0^{2\pi}\frac{\mu(e')\, z_e(e')\,[\tilde{q}(e)-\tilde{q}(e')]}{\sin^2\tfrac{1}{2}[z(e)-z(e')]}\,de'. \tag{2.17}$$

Since $\partial\Phi/\partial t$ involves an integral of $\partial\mu/\partial t$, (2.14) is a Fredholm integral equation of the second kind for $\partial\mu/\partial t$. Similarly, an integral expression for $\partial q^*/\partial t$ is easily obtained that makes (2.15) a Fredholm equation of the second kind for $\partial\gamma/\partial t$.

The basis for the methods advocated in this paper is that (2.14) has a globally convergent Neumann series. To prove this we follow Bergman & Schiffer (1953). First

we rewrite (2.14) as

$$\frac{\partial \mu}{\partial t}(e) = -\frac{\lambda}{2\pi} \mathrm{P} \int_0^{2\pi} \frac{\partial \mu}{\partial t}(e') \operatorname{Im}\{z_e(e') \cot \tfrac{1}{2}[z(e)-z(e')]\}\, de' + r(e), \tag{2.18}$$

to show explicitly the nature of the Fredholm equation, where $\lambda = A$. Here $r(e)$ contains all terms not dependent on $\partial\mu/\partial t$. For the Neumann series to converge, the value of λ must be smaller than the absolute value of any eigenvalue λ_n of the integral equation

$$X_n(e) = -\frac{\lambda_n}{2\pi} \mathrm{P} \int_0^{2\pi} X_n(e') \operatorname{Im}\{z_e(e') \cot \tfrac{1}{2}[z(e)-z(e')]\}\, de'. \tag{2.19}$$

Note that λ_n and $X_n(e)$ may be complex.

Next, define the complex harmonic function

$$\begin{aligned} w &= w_{\mathrm{r}} + i w_{\mathrm{i}} \\ &= -\frac{1}{4\pi} \int_0^{2\pi} X_n(e') \operatorname{Im}\{z_e(e') \cot \tfrac{1}{2}[z-z(e')]\}\, de'. \end{aligned} \tag{2.20}$$

The real and imaginary functions w_{r} and w_{i} are harmonic in the regions above and below the interface (but w is not necessarily analytic). The jump of w at the interface is X_n, so that the limiting values of w are

$$w_1 = \frac{1}{2}\left[\frac{1}{\lambda_n} - 1\right] X_n, \tag{2.21}$$

$$w_2 = \frac{1}{2}\left[\frac{1}{\lambda_n} + 1\right] X_n, \tag{2.22}$$

where we have made use of (2.19) to eliminate the principal-value integral. Using Green's first identity on the complex harmonic function w, the continuity of the normal derivatives of w_1 and w_2, and (2.21) and (2.22), we obtain

$$\iint_{R_1} \nabla w \cdot \nabla w^*\, dA = -\frac{1}{2}\left[\frac{1}{\lambda_n} - 1\right] \int_0^{2\pi} X_n(e) \frac{\partial w^*}{\partial \nu} s_e\, de, \tag{2.23}$$

$$\iint_{R_2} \nabla w \cdot \nabla w^*\, dA = -\frac{1}{2}\left[\frac{1}{\lambda_n} + 1\right] \int_0^{2\pi} X_n(e) \frac{\partial w^*}{\partial \nu} s_e\, de. \tag{2.24}$$

The semi-infinite regions R_1 (R_2) have width 2π and lie below (above) the interface, and ν is normal to the interface pointing into the region R_2. The integrals on the left-hand side of (2.23) and (2.24) are positive, so that

$$\left(1 - \frac{1}{\lambda_n^2}\right)\left(\int_0^{2\pi} X_n \frac{\partial w^*}{\partial \nu} s_e\, de\right)^2 \geqslant 0. \tag{2.25}$$

On the other hand, adding (2.23) and (2.24) shows that the integral in (2.25) is real. Since the integral in (2.25) does not vanish, it follows that λ_n is real with

$$\lambda_n^2 > 1. \tag{2.26}$$

In periodic semi-infinite geometry, neither $\lambda_n = \pm 1$ is an eigenvalue.

At the interface it is necessary to evaluate the integrals corresponding to the potential or velocity in the sense of a principal value. These principal-value integrals may be made regular by the appropriate subtraction of a known principal-value

integral. Recalling the identity

$$\int_0^{2\pi} \cot\tfrac{1}{2}[z(e)-z(e')]\frac{dz}{de'}(e')\,de' = 0,$$

we rewrite (2.3) and (2.6) evaluated at the interface in the non-singular forms

$$\Phi(e) = \frac{1}{4\pi i}\int_0^{2\pi} [\mu(e')-\mu(e)]\cot\tfrac{1}{2}[z(e)-z(e')]\frac{dz}{de'}(e')\,de', \tag{2.27}$$

$$q^*(e) = \frac{1}{4\pi i}\int_0^{2\pi} \frac{\gamma(e')\,z_e(e)-\gamma(e)\,z_e(e')}{z_e(e)}\cot\tfrac{1}{2}[z(e)-z(e')]\,de'. \tag{2.28}$$

The expressions for $\partial\Phi/\partial t$ (see (2.17)) and $\partial q^*/\partial t$ also contain principal-value integrals. These integrals are regularized by differentiating (2.27) and (2.28) with respect to t, avoiding use of (2.3) and (2.6).

These integrals may be accurately evaluated numerically by the trapezoidal rule (see e.g. Baker 1980). Derivatives with respect to e are usually computed using cubic spline approximations. In practice, we have found that for highly distorted periodic geometries, the dipole form (2.27) gives more-accurate and instability-free results. Numerically, the vortex form (2.28) is more susceptible to round-off. As $e \to e'$ cancellation occurs due to the presence of the derivative term z_e in the integrand, which is less accurately known.

To summarize, the numerical procedure using the dipole representation is as follows. First the complex potential $\Phi(e)$ is calculated from (2.3). Then the complex velocity $q(e)$ is obtained from (2.5) and the interface is marched forward using (2.7). Next the inhomogeneous term $r(e)$ in (2.18) is evaluated from (2.14) and (2.17). Finally, (2.18) is solved (by accelerated iteration) for $\partial\mu/\partial t$ so that μ can also be marched in time. This completes a time step. The time-stepping is actually performed using a fourth-order Adams–Moulton predictor–corrector scheme. A similar procedure is used to march the vortex sheet equations in time in cases (like those involving radiation boundary conditions) where vortex layers seem computationally more practical than dipole layers.

3. Application to steady and unsteady surface and interfacial waves

A simple but non-trivial test of the time-dependent numerical scheme is obtained by calculating the propagation of steady interfacial waves. The initial wave profiles and vortex-sheet strength are obtained by solving the nonlinear equations (A 2)–(A 5) derived in the appendix for Atwood ratios $A = 1{\cdot}0$ (a surface wave) and $A = 0{\cdot}8181$. The wave heights are chosen to be $h = 0{\cdot}4$ ($A = 1{\cdot}0$) and $0{\cdot}36$ ($A = 0{\cdot}8181$), where h is the average of the crest and trough amplitudes so both test cases correspond to nonlinear waves. Also, we choose $g = 1$.

The accuracy of the time-dependent solution is checked by comparing the locations of the markers with the exact solution at time $t = 0$ translated in the x-direction by an amount ct, where c is the nonlinear phase speed of the wave. Numerical solution of the nonlinear integral equations (A 2)–(A 5) gives $c = 1{\cdot}082$ for the surface wave and $c = 0{\cdot}952$ for the interfacial wave. The results obtained by time integration of the equations of §2 using $N = 128$ points and a time step $\Delta t = \frac{2}{400}\pi$ are plotted in figures 2 and 3 at $t = 0, 2\pi$ when the waves have propagated through about one period. At these times the numerical and theoretical profiles agree to one part in 10^4.

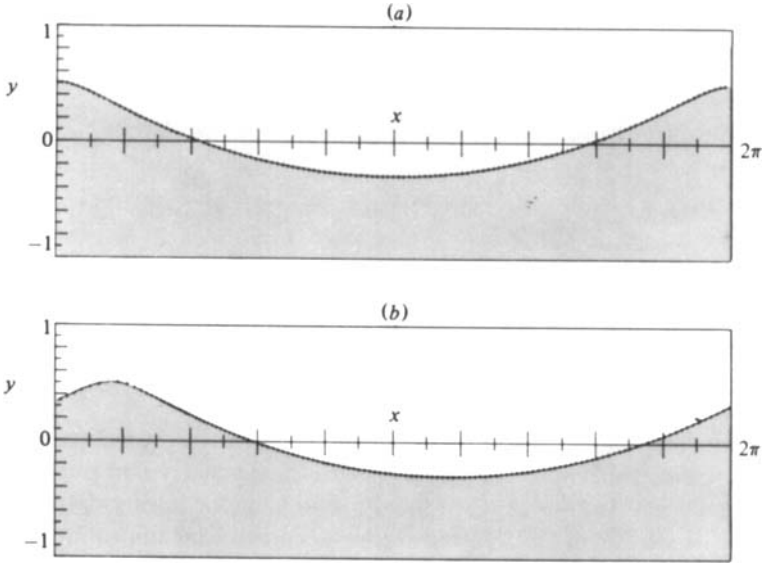

FIGURE 2. A plot of the Stokes wave profile ($A = 1$) at times (*a*) $t = 0$ and (*b*) $t = 2\pi$. The dots indicate the numerically computed position of the interface. The solid line is obtained by solving the nonlinear integral equations (A 2)–(A 5).

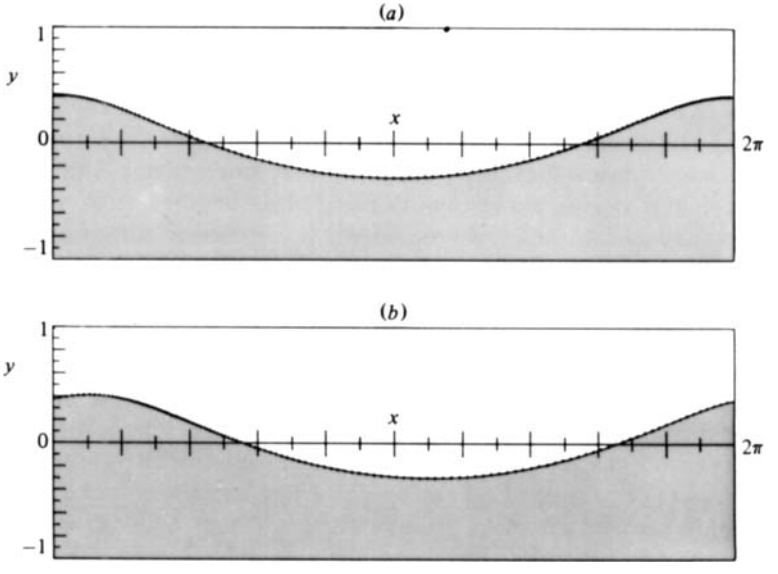

FIGURE 3. Same as figure 2 except $A = 0{\cdot}8182$.

There are several invariants of the flow. In particular, there is an invariant associated with conservation of energy. Strictly speaking, the total energy for two-dimensional stratified flow is infinite. However, the perturbation energy of the disturbed flow away from a steady-state value, evaluated over one spatial period of the flow, is finite and conserved. This perturbed energy provides a useful diagnostic on the numerical computation. The perturbation kinetic energy is given by

$$E_{\mathrm{K}} = \tfrac{1}{2}\rho_2 \int_{R_2} \int (u^2+v^2)\, dA + \tfrac{1}{2}\rho_1 \int_{R_1} \int (u^2+v^2)\, dA,$$

where R_1 and R_2 are defined after (2.24). Using Green's theorem E_K may be rewritten as a boundary integral:

$$E_K = -\tfrac{1}{2}\rho_1 \int_0^{2\pi} \frac{\partial \psi_1}{\partial \nu} \psi s_e \, de + \tfrac{1}{2}\rho_2 \int_0^{2\pi} \frac{\partial \psi_2}{\partial \nu} \psi s_e \, de,$$

so that

$$\frac{4E_K}{\rho_1 + \rho_2} = \int_0^{2\pi} \psi \gamma \, de + 2A \int_0^{2\pi} \psi \phi_e \, de.$$

Here ψ and ϕ are respectively the average stream function and potential, and we use the fact that the stream function is continuous at the interface. The perturbation potential energy E_P is given by

$$\frac{4E_P}{\rho_1 + \rho_2} = +2Ag \int_0^{2\pi} y^2 x_e \, de.$$

Thus the total perturbation energy E is

$$\frac{4E}{\rho_1 + \rho_2} = \int_0^{2\pi} \psi \gamma \, de + 2A \left[\int_0^{2\pi} \psi \phi_e \, de + g \int_0^{2\pi} y^2 x_e \, de \right]. \tag{3.1}$$

The equations of motion show that E is conserved in time. For the simulations of steady waves with $N = 128$ and $\Delta t = \frac{2}{400}\pi$, energy is conserved to better than one part in 10^4 through several wave periods.

The application of fourth-order polynomial extrapolation techniques in time (using 4 previous time levels) allows the computation of $\partial\gamma/\partial t$ or $\partial\mu/\partial t$ to a tolerance of 10^{-8} with just 2 iterations per predictor–corrector step. Thus the operation count is truly $O(N^2)$.

In their simulations of steady nonlinear surface waves, Longuet-Higgins & Cokelet (1976) observed the onset of a high-wavenumber instability as the wave progressed forward in time. This instability was removed by a five-point smoothing operator applied every five time steps or so. Our simulations also suffer from this weak instability when vortex markers are used. In contrast, no such instability has been observed in similar runs by Vinje & Brevig (1981). This may be due to numerical diffusion introduced by their finite-difference scheme.

When dipole markers are used, it is apparently not necessary to smooth, presumably because the subtraction in (2.27) can be implemented more accurately than that in (2.28). In our dipole simulations (which also have spectral accuracy) it has been possible to increase the time over which the code simulates waves accurately without any smoothing by simply increasing the number of markers. With 128 points, the Stokes wave travels over 2·5 wavelengths before the onset of the high-wavenumber instability. It may be concluded that, for surface waves, smoothing is not required in the dipole equations provided that a sufficiently large number of markers is used to resolve the interface.

While surface waves apparently do not require smoothing, a strong instability has been observed in the case of travelling interfacial waves of permanent form. The origin of this instability of the dipole equations may be a real physical instability of the local shear layers in the interfacial wave. This phenomenon is now under detailed study.

Having demonstrated the reliability of the iterative vortex method for finite-amplitude steady flows, we show that the method is capable of following unsteady waves well into the breaking regime. We have used as an initial condition a Stokes

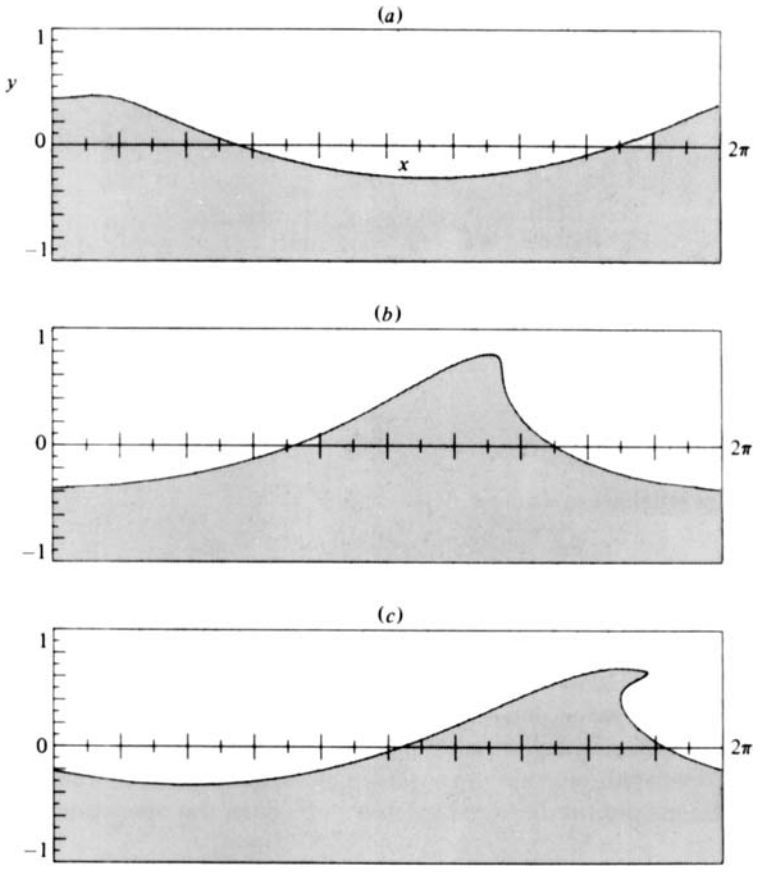

FIGURE 4. A plot at various times of the profile of a breaking wave on infinite depth. The height of the Stokes wave used as an initial condition is 80% of the maximum. The wave is forced by a moving pressure pulse of the form $p(x,t) = p_0 \sin t \sin(x-ct)$, with $p_0 = 0{\cdot}146$. The pressure pulse is turned off after $t = \pi$. The profile is shown at times (*a*) $t = 0{\cdot}38$, (*b*) $t = 3{\cdot}16$ and (*c*) $t = 4{\cdot}22$. Note that in (*c*) the wave has broken and a smooth jet has been ejected from the forward face of the wave.

wave that is 80% of maximum height. A pressure distribution of the form

$$p_s(x,t) = p_0 \sin t \sin(x-ct)$$

is applied at times $0 \leqslant t \leqslant \pi$ and is switched off at $t = \pi$. Thus the energy is increased smoothly until $t = \pi$. This run is similar to the case considered by Longuet-Higgins & Cokelet (1976). As is seen in figure 4 the wave overturns and a jet of fluid is ejected from the forward face of the wave. The iterative method continues to converge until the curvature at the tip becomes too great to resolve with the number of points used (see also Vinje & Brevig 1981).

4. Bottom topography

Flows such as those generated by surface waves over bottom topography or due to a solid body in motion underneath an interface require Neumann boundary conditions at the solid boundaries in addition to the free-surface conditions. Since the fluid cannot penetrate a solid boundary, the normal fluid velocity at the body must equal the normal body velocity.

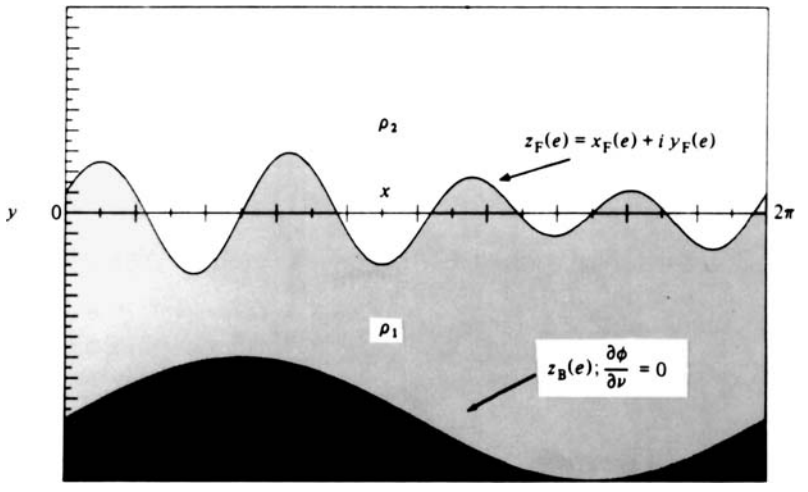

FIGURE 5. Flow geometry for interfacial flow with bottom topography.

All potential fields may be constructed by means of surface distributions of sources and dipoles. It was shown in §2 that potential flows with Dirichlet boundary conditions may be expressed as those due to a distribution of dipoles or vortices. The dipole-layer potential has jump discontinuities, but its normal derivative varies continuously as the surface or interface is penetrated along the normal. In contrast, the potential due to a layer of sources varies continuously as the surface is penetrated, but the normal derivative has a jump discontinuity. Thus it is natural to impose a distribution of sources along the solid boundary to obtain an irrotational flow with Neumann boundary conditions. Indeed, the use of source distributions to solve the Neumann problem again leads to Fredholm integral equations of the second kind. The kernels of these equations retain the property that the largest eigenvalue is less than unity in absolute value† so that the iteration methods discussed in §2 continue to work.

The bottom boundary and interfaces are assumed to be 2π-periodic in the horizontal direction. It is necessary to consider only one interface above the solid bottom since the generalization to several interfaces is straightforward. Using the complex variables introduced in §2, we parametrize the free surface and solid boundary by $z_F(e)$ and $z_B(e)$ respectively, with $0 \leqslant e \leqslant 2\pi$ (see figure 5). The bottom is assumed stationary, a condition that may be easily relaxed.

Let the dipole strength and source strength associated with the free surface and solid boundary be $\mu_F(e)$ and $\sigma(e)/s_e(e)$, $s_e^2 = z_{Be}\, z_{Be}^*$ respectively. The complex potential may be written as

$$\Phi(z) = \frac{1}{4\pi i}\int_0^{2\pi} \mu_F(e)\, z_{fe}(e) \cot \tfrac{1}{2}[z - z_F(e)\, de + \frac{1}{2\pi}\int_0^{2\pi} \sigma(e) \log[\sin \tfrac{1}{2}[z - z_B(e)]]\, de. \tag{4.1}$$

Defining $\sigma(e) = \mu_{Be}(e)$ and integrating by parts, we find

$$\Phi(e) = \frac{1}{4\pi i}\int_0^{2\pi} \mu_F(e)\, z_{Fe}(e) \cot \tfrac{1}{2}[z - z_F(e)]\, de + \frac{1}{4\pi}\int_0^{2\pi} \mu_B(e)\, z_{Be}(e) \cot \tfrac{1}{2}[z - z_B(e)]\, de. \tag{4.2}$$

† See Schiffer (1959) for a discussion of the distribution of eigenvalues in multiple connected domains.

As in §2, we define the complex velocity of the free surface as

$$\frac{\partial z_{\mathrm{F}}^*(e)}{\partial t} = \tilde{q}^*(e) = q^*(e) + \frac{\alpha\gamma(e)}{2z_{\mathrm{F}e}(e)}, \tag{4.3}$$

where $q^*(e) = \Phi_e/z_{\mathrm{F}e}(e)$, $\gamma(e) = \mu_{\mathrm{F}e}(e)$, and $\Phi(e)$ is the average complex potential at the interface obtained by taking the principal value of the integrals (4.1), (4.2). The complex velocity may also be expressed in terms of γ and σ as

$$q^*(e) = \frac{1}{4\pi i}\mathrm{P}\int_0^{2\pi} \gamma(e')\cot\tfrac{1}{2}[z_{\mathrm{F}}(e)-z_{\mathrm{F}}(e')]\,de' + \frac{1}{4\pi}\int_0^{2\pi} \sigma(e')\cot\tfrac{1}{2}[z_{\mathrm{F}}(e)-z_{\mathrm{B}}(e')]\,de. \tag{4.4}$$

The evolution equation (2.14) for μ_{F} is

$$\frac{\partial \mu_{\mathrm{F}}}{\partial t} - \frac{\alpha\gamma^2}{2z_{\mathrm{F}e}z_{\mathrm{F}e}^*} = -2A\left[\mathrm{Re}\left\{\frac{\partial\Phi}{\partial t}\right\} - \tfrac{1}{2}q^*q - \tfrac{1}{2}\alpha\gamma\,\mathrm{Re}\left\{\frac{q}{z_{\mathrm{F}e}}\right\} + \frac{1}{8}\frac{\gamma^2}{z_{\mathrm{F}e}z_{\mathrm{F}e}^*} + gy_{\mathrm{F}}\right], \tag{4.5}$$

where A is the Atwood ratio (see (2.16)) for the interface. Differentiating (4.2) with respect to time gives

$$\begin{aligned}\frac{\partial\Phi(e)}{\partial t} = {} & \frac{1}{4\pi i}\mathrm{P}\int_0^{2\pi}\left(\frac{\partial\mu_{\mathrm{F}}}{\partial t}(e')\,z_{\mathrm{F}e}(e') + \mu_{\mathrm{F}}(e')\,\tilde{q}_e(e')\right)\cot\tfrac{1}{2}[z_{\mathrm{F}}(e)-z_{\mathrm{F}}(e')]\,de' \\ & - \frac{1}{8\pi i}\mathrm{P}\int_0^{2\pi}\frac{\mu_{\mathrm{F}}(e')\,(\tilde{q}(e)-\tilde{q}(e'))}{\sin^2\tfrac{1}{2}[z_{\mathrm{F}}(e)-z_{\mathrm{F}}(e')]}z_{\mathrm{F}e}(e')\,de' \\ & + \frac{1}{4\pi}\int_0^{2\pi}\frac{\partial\mu_{\mathrm{B}}}{\partial t}(e')\,z_{\mathrm{B}e}(e')\cot\tfrac{1}{2}[z_{\mathrm{F}}(e)-z_{\mathrm{B}}(e')]\,de' \\ & - \frac{1}{8\pi}\int_0^{2\pi}\frac{\mu_{\mathrm{B}}(e')\,z_{\mathrm{B}e}(e')\,\tilde{q}(e)}{\sin^2\tfrac{1}{2}[z_{\mathrm{F}}(e)-z_{\mathrm{B}}(e')]}de'.\end{aligned} \tag{4.6}$$

The evolution equation (2.15) for γ involves $\partial q^*/\partial t$, which may be obtained by differentiating (4.4) in time. To close the system (4.1)–(4.6), we require evolution equations for σ or μ_{B}.

As yet we have not imposed the condition that the normal velocity vanishes at the solid bottom. This condition, which is $\mathrm{Im}\{z_{\mathrm{B}e}q_{\mathrm{B}}^*\} = 0$, where q_{B}^* is the fluid velocity at the boundary, provides the necessary evolution equations for σ and μ_{B}. Indeed, $\mathrm{Im}\{z_{\mathrm{B}e}q_{\mathrm{B}}^*\} = 0$ implies

$$\begin{aligned}\sigma(e) = 2\,\mathrm{Im}\{z_{\mathrm{B}e}(e)\Big[& \frac{1}{4\pi i}\int_0^{2\pi}\gamma(e')\cot\tfrac{1}{2}[z_{\mathrm{B}}(e)-z_{\mathrm{F}}(e')]\,de' \\ & + \frac{1}{4\pi}\mathrm{P}\int_0^{2\pi}\sigma(e')\cot\tfrac{1}{2}[z_{\mathrm{B}}(e)-z_{\mathrm{B}}(e')]\,de'\Big]\Big\}.\end{aligned} \tag{4.7}$$

Alternatively, the stream function must be a constant (zero for convenience) along the interface. Thus

$$\begin{aligned}\mu_{\mathrm{B}}(e) = 2\,\mathrm{Im}\Big\{ & \frac{1}{4\pi i}\int_0^{2\pi}\mu_{\mathrm{F}}(e')\,z_{\mathrm{F}e}(e')\cot\tfrac{1}{2}[z_{\mathrm{B}}(e)-z_{\mathrm{F}}(e')]\,de' \\ & + \frac{1}{4\pi}\mathrm{P}\int_0^{2\pi}\mu_{\mathrm{B}}(e')\,z_{\mathrm{B}e}(e')\cot\tfrac{1}{2}[z_{\mathrm{B}}(e)-z_{\mathrm{B}}(e')]\,de'\Big\}.\end{aligned} \tag{4.8}$$

Differentiating (4.8) with respect to e also gives (4.7). Finally, differentiating (4.7)

and (4.8) with respect to time gives

$$\frac{\partial\sigma(e)}{\partial t} = 2\,\mathrm{Im}\left\{z_{\mathrm{B}e}(e)\left[\frac{1}{4\pi i}\int_0^{2\pi}\frac{\partial\gamma(e')}{\partial t}\cot\tfrac{1}{2}[z_{\mathrm{B}}(e)-z_{\mathrm{F}}(e')]\,de'\right.\right.$$
$$\left.\left.+\frac{1}{8\pi i}\int_0^{2\pi}\frac{\gamma(e')\,\tilde{q}(e')\,de'}{\sin^2\tfrac{1}{2}[z_{\mathrm{B}}(e)-z_{\mathrm{F}}(e')]}+\frac{1}{4\pi}\mathrm{P}\int_0^{2\pi}\frac{\partial\sigma}{\partial t}(e')\cot\tfrac{1}{2}[z_{\mathrm{B}}(e)-z_{\mathrm{B}}(e')]\,de'\right]\right\}, \tag{4.9}$$

$$\frac{\partial\mu_{\mathrm{B}}(e)}{\partial t} = 2\,\mathrm{Im}\left\{\frac{1}{4\pi i}\int_0^{2\pi}\left[\frac{\partial\mu_{\mathrm{F}}}{\partial t}(e')\,z_{\mathrm{F}e}(e')+\mu_{\mathrm{F}}(e')\,\tilde{q}_e(e')\right]\cot\tfrac{1}{2}[z_{\mathrm{B}}(e)-z_{\mathrm{F}}(e')]\,de'\right.$$
$$+\frac{1}{8\pi i}\int_0^{2\pi}\frac{\mu_{\mathrm{F}}(e)\,z_{\mathrm{F}e}(e')\,\tilde{q}(e')\,de'}{\sin^2\tfrac{1}{2}[z_{\mathrm{B}}(e)-z_{\mathrm{F}}(e')]}$$
$$\left.+\frac{1}{4\pi}\mathrm{P}\int_0^{2\pi}\frac{\partial\mu_{\mathrm{B}}}{\partial t}(e')\,z_{\mathrm{B}e}(e')\cot\tfrac{1}{2}[z_{\mathrm{B}}(e)-z_{\mathrm{B}}(e')]\,de'\right\}. \tag{4.10}$$

Equations (4.2), (4.3), (4.5), (4.6) and (4.10) are a set of evolution equations for z_{F}, μ_{F} and μ_{B}. The equations for $\partial\mu_{\mathrm{F}}/\partial t$ and $\partial\mu_{\mathrm{B}}/\partial t$ are coupled Fredholm integral equations of the second kind and may be solved iteratively. Alternatively, (4.3), (4.4), (4.9) together with equations for $\partial\gamma/\partial t$ and $\partial q^*/\partial t$ are the evolution equations for a vortex-sheet–source representation of the free surface and solid boundary. In both cases the principal-value integrals may be regularized and the equations solved numerically as outlined in §2.

The rate of convergence of the iteration procedure for coupled integral equations like (4.5) and (4.10) is somewhat slower than for the case of infinite depth described in §2. For infinite depth (corresponding to a simply connected domain) the largest eigenvalue is essentially a function of the aspect ratio of the geometry. For finite depth, which corresponds to a doubly connected domain, the largest eigenvalue can be related to the depth-to-wavelength ratio. As the geometry becomes shallower the dominant eigenvalue tends toward 1. Indeed, for linear shallow-water theory the dominant eigenvalue is $O(\exp(-kd))$, where d is the depth. Because of this, a larger number of iterations are needed in the initial stages of the integration forward in time. However, once a sufficient number of previous time levels are known, extrapolation schemes may be used to reduce the number of iterations to only two or three per time step.

In all runs made with this method we used 128 points on the free surface and 128 on the bottom. An equivalent simulation using Green's third formula would entail the inversion of a 256×256 matrix at each time step. The use of fewer points results in inadequate resolution of regions of large curvature at the interface. With 128 markers on the free surface and on the bottom, our iterative methods require only about 0·1 s per time step on a Cray-1 computer.

Next we report results obtained by applying the dipole–source technique to the calculation of periodic surface waves over periodic bottom topography. The initial conditions for all the nonlinear runs reported below are

$$\left.\begin{aligned} &x(e,t=0) = e, \quad y(e,t=0) = a\cos e, \quad x_{\mathrm{B}}(e) = e, \quad y_{\mathrm{B}}(e) = -d+b\sin e,\\ &\gamma(e,t=0) = a(\tanh d)^{-\frac{1}{2}}(1+\tanh d)\cos e, \quad \sigma(e,t=0) = -a(\tanh d)^{-\frac{1}{2}}\sin e. \end{aligned}\right\} \tag{4.11}$$

For small values of the amplitude a and $b = 0$ these conditions correspond to a linear wave that propagates to the right at the speed $(\tanh d)^{\frac{1}{2}}$. The period of the linear wave

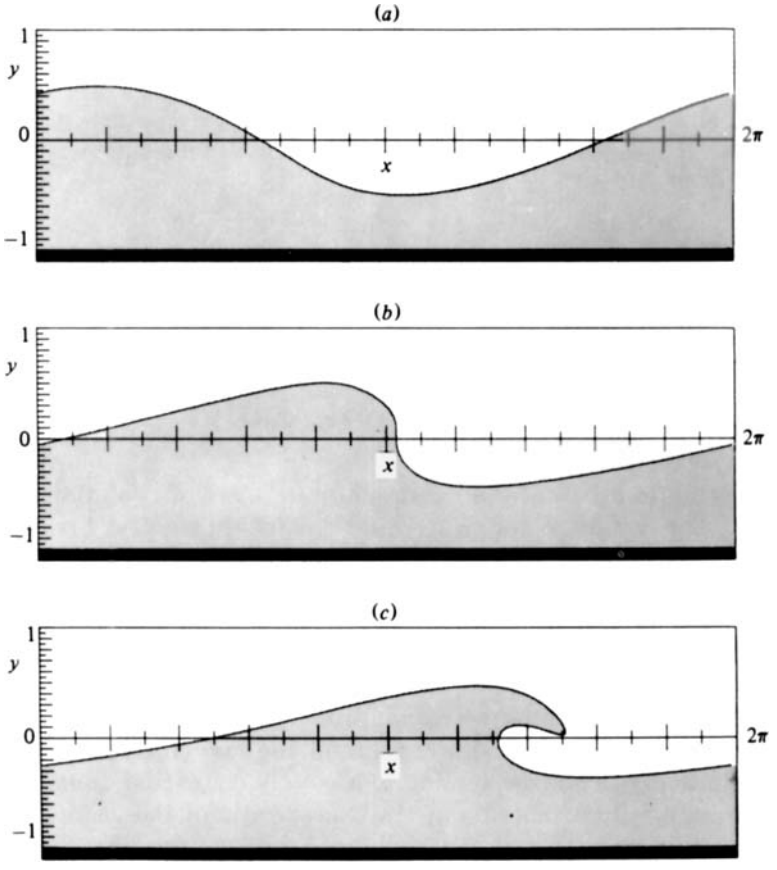

FIGURE 6. A plot at various times of the profile of a plunging breaker on finite depth. The initial condition corresponds to a cosine wave with a large initial amplitude $a = 0{\cdot}5$ (see (4.11)). The wave is plotted at times (*a*) $t = 0{\cdot}46$, (*b*) $t = 1{\cdot}85$, and (*c*) $t = 3{\cdot}1$.

is $t_0 = 2\pi\,(\tanh d)^{-\frac{1}{2}}$. In order to simulate a plunging breaker we choose $a = 0{\cdot}5$, $d = 1$ and $b = 0$. The results are plotted in figure 6. At time $t = 0{\cdot}26t_0 \approx 1{\cdot}85$ the profile has become vertical, and at $t = 0{\cdot}43t_0 \approx 3{\cdot}1$ a jet has been ejected from the forward face of the crest. The profile is similar to that of a plunging breaker.

A spilling breaker is generated by the initial conditions $a = 0{\cdot}2$, $d = 0{\cdot}5$ and $b = 0{\cdot}1$. This is a slightly unsteady wave propagating over a sinusoidal bottom. A sequence of wave profiles is plotted in figure 7. At $t = 0{\cdot}43t_0 \approx 4{\cdot}0$ the wave crest is spilling.

The dipole–source technique is also capable of simulating motion over more distorted topographies. In figure 8 we plot the time evolution of a wave with initial conditions $d = -0{\cdot}5$, $a = 0{\cdot}2$ and $b = -0{\cdot}1$ in (4.11), but with a bottom x-coordinate parametrized as

$$x_{\mathrm{B}}(e) = e - \sin e.$$

The bottom therefore resembles a rising step. The technique gives reliable wave profiles well after the wave crest has become vertical.

In order to provide a more detailed picture of the dynamics of the plunging breaker we have examined the velocities and accelerations of the fluid surface. Following Peregrine, Cokelet & McIver (1980), we plot a phase (hodograph) plane of the surface x-velocity versus the y-velocity. By drawing the radius vector to any point on this

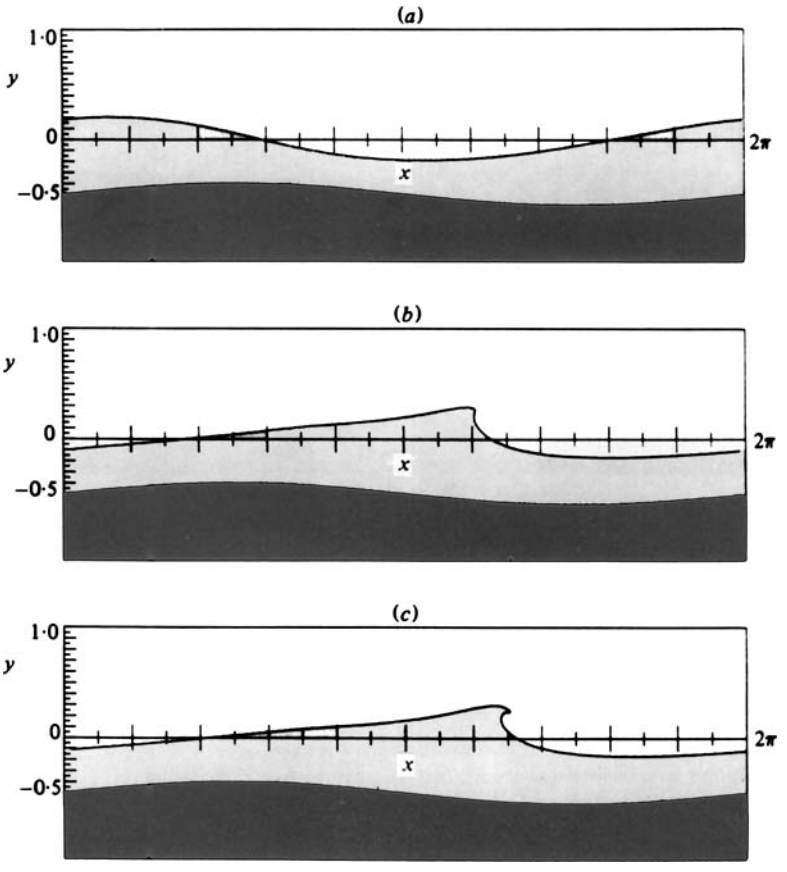

FIGURE 7. A plot at various times of the profile of a spilling breaker. The initial condition corresponds to a cosine wave with initial amplitude $a = 0{\cdot}2$. The bottom topography has the form $z_B = e + i(-0{\cdot}5 + 0{\cdot}1 \sin e)$. The wave is plotted at times (*a*) $t = 0{\cdot}46$, (*b*) $t = 3{\cdot}70$ and (*c*) $t = 4{\cdot}0$.

hodograph plane the magnitude and direction of the velocity may be deduced. We plot the results for the plunging wave (see figure 6) in figure 9. The curves are plotted at time intervals of $\frac{1}{20}t_0$, where $t_0 = 2\pi\,(\tanh 1)^{-\frac{1}{2}} \approx 7{\cdot}2$. The crest of the wave is located at the rightmost point of the hodograph, while the trough corresponds to the leftmost point. The front (back) of the wave corresponds to the upper (lower) half of the elliptical curves. As the wave steepens, the velocities at the crest increase. At the point of plunging the crest velocities point downwards toward the interface. The magnitudes of the velocities in the forward jet are greater than the nonlinear phase speed of the highest Stokes wave at this depth.

The accelerations for this plunging breaker are plotted in figure 10. At early times the acceleration is essentially orthogonal to the velocity vector. The front and back of the travelling wave now correspond to the rightmost and leftmost points respectively of the elliptical profiles, while the crest and trough are located at the bottom and top.

As the wave approaches breaking, the surface profiles of acceleration depart markedly from the steady state shown in figure 10. The largest accelerations are located in the region just below the crest. These accelerations are at least four to five times larger than the acceleration due to gravity and are pointed in the forward

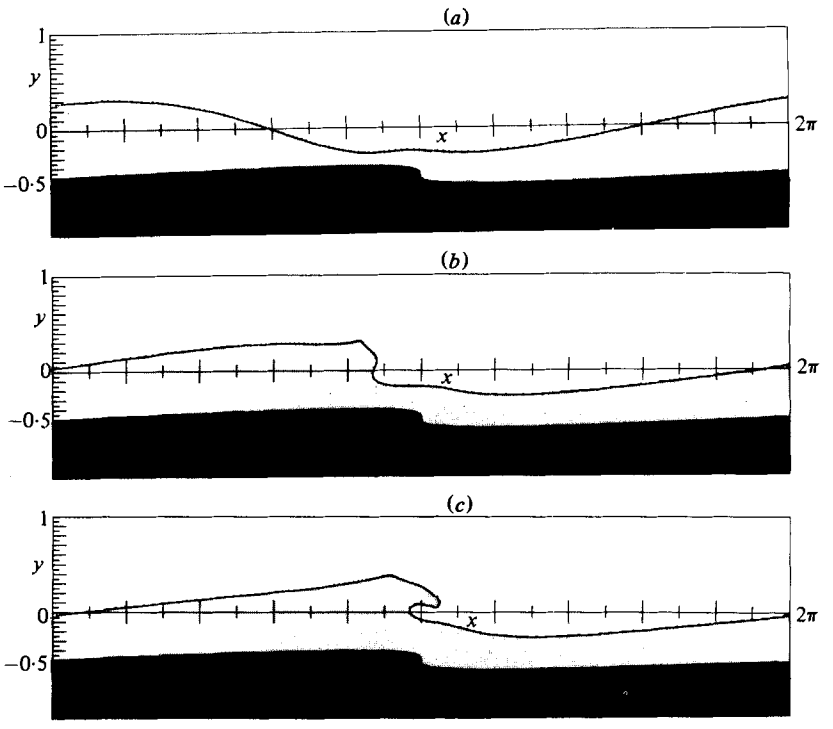

FIGURE 8. A plot at various times of the profile of a breaker over a descending step. The initial conditions correspond to a cosine wave with initial amplitude $a = 0{\cdot}2$. The bottom topography has the form $z_B = (e - \sin e) + i\,(-0{\cdot}5 - 0{\cdot}1 \sin e)$. The wave is plotted at times (*a*) $t = 0{\cdot}46$, (*b*) $t = 1{\cdot}84$ and (*c*) $t = 2{\cdot}472$.

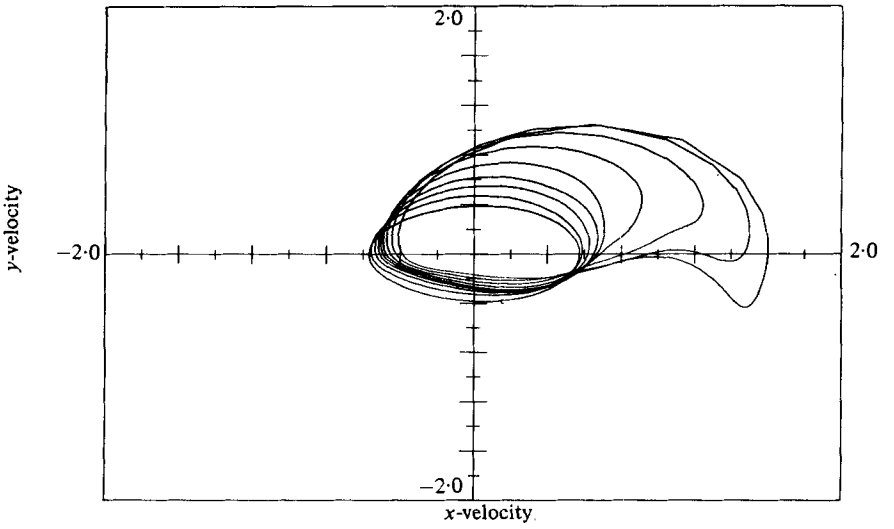

FIGURE 9. A phase portrait of the y-velocity versus the x-velocity for the plunging breaker shown in figure 6.

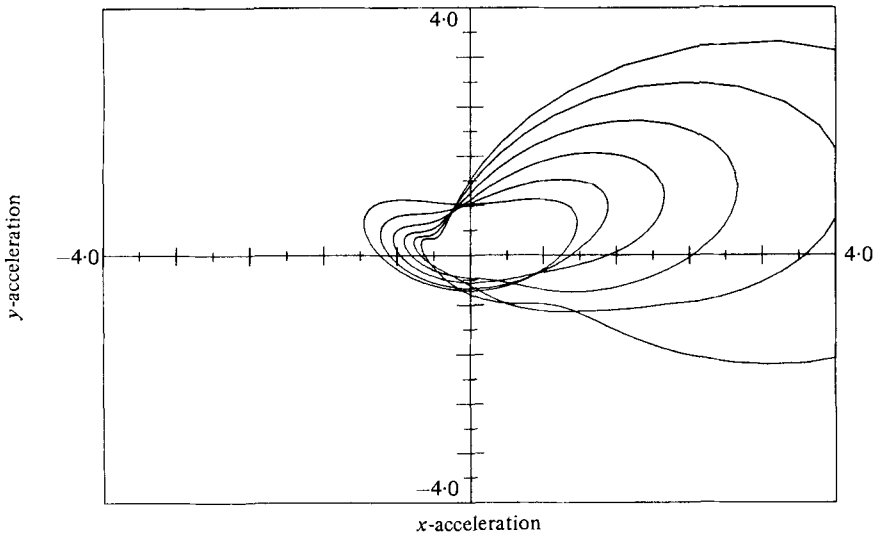

FIGURE 10. A phase portrait of the y-acceleration versus the x-acceleration for the plunging breaker shown in figure 6. The free-fall point is located at (0·0, −1·0).

direction. Peregrine *et al.* have also observed large accelerations in the crest region in qualitative agreement with our results.

Despite the large forward accelerations observed just under the crest of the breaker, the tip of the wave appears to be in free fall. At time $t = 0{\cdot}28$, $t_0 \approx 2{\cdot}0$ the acceleration at the tip exceeds g (1·0 in our units) by approximately 30%. The forward face of the wave is essentially vertical at this time. At later times the acceleration at the tip decreases to 1·0. Indeed, at $t = 0{\cdot}41$, $t_0 \approx 2{\cdot}97$ there is a region about the tip in which the fluid accelerations vary by less than five per cent from the free-fall value. In this region the acceleration vectors within the same level of variation point in the $-y$-direction.

The qualitative similarity of our results with those of Peregrine *et al.* indicates that the flow in the plunging region of breakers is a local phenomenon. The remainder of the wave is subject to relatively low accelerations and does not appear to influence the dynamics of the plunging jet.

Longuet-Higgins (1981) has recently proposed several analytic forms for the complex potential in the breaking region. A detailed comparison between this theoretical approach and the numerical approach of this section is currently under way.

5. Resonant interaction of surface and interfacial gravity waves

Triad resonant interactions between surface and interfacial gravity waves in a stratified fluid account for some of the energy transfer from wind-driven surface waves to internal waves. Among others, Hasselman (1966) and Watson, West & Cohen (1976) have attempted to include the effect of resonant triad interactions in their study of ocean dynamics, but the work is based on weakly nonlinear perturbation theory and the conditions under which the perturbation analysis is valid are not yet clear. By considering a simple model of the ocean, we can use our numerical technique

to study nonlinear triad resonant interactions and shed some light on the accuracy of the perturbation analyses.

We assume that the ocean consists of two layers of incompressible, irrotational, inviscid fluid of constant, but different, densities. The top layer has density ρ' and thickness d, while the bottom layer has density $\rho > \rho'$ and is infinitely deep. Although this model of the ocean is rather simple, it has been used before in studies of ocean dynamics by Ball (1964), Kenyon (1966), and others. Moreover, Craik & Adam (1979) have applied weakly nonlinear perturbation theory to stratified three-layer fluid flow.

Using the notation of Craik & Adam (1979), we choose $\rho_1 = 0$, $\rho_2 = \rho' = 0{\cdot}787\,775$, $\rho_3 = 1$, $u_1 = u_2 = u_3 = 0$, $\gamma_1 = \gamma_2 = 0$, $d = 1$ and $g = 1$. The three modes that form a resonant triad are given by wavenumbers $k_1 = 3$, $k_2 = 1$, $k_3 = 2$ and frequencies $\omega_1 = \sqrt{3}$ (a surface wave), $\omega_2 = \sqrt{3} - \sqrt{2}$ (an interfacial wave), $\omega_3 = \sqrt{2}$ (a surface wave) respectively. Our choice of the above parameters was guided by several considerations. First, we require that the wavenumbers be small so that the numerical computation of the evolution of the interface does not require an excessive number of markers. Secondly, we require that the timescale for the resonant interaction be reasonably small so that the computation can be done relatively quickly. Finally, we choose integer values for the wavenumbers consistent with a spatial periodicity of 2π.

We denote the complex amplitudes of the surface elevation ($A_1^{(j)}$ in Craik & Adam's notation) corresponding to the three modes as $A_1^{(1)} = a_3$, $A_1^{(2)} = -ia_1$, $A_1^{(3)} = a_2$ so that the subscript on a refers directly to the value of the wavenumber. Direct substitution into the evolution equations for the complex amplitudes (equation (4.3) in Craik & Adam) gives the following system:

$$\frac{da_1}{dt} = 0{\cdot}026\,88a_2a_3, \quad \frac{da_2}{dt} = 3{\cdot}384a_1a_3, \quad \frac{da_3}{dt} = -4{\cdot}162a_1a_2. \tag{5.1}$$

For initial conditions, we take $a_1(0) = 0$, $a_2(0) = \epsilon$ and $a_3(0) = \frac{2}{3}\epsilon$; thus the surface waves have the property that $ak = 2\epsilon$ initially. The system (5.1) may be solved exactly in terms of elliptic functions:

$$a_1 = 0{\cdot}049\,52\epsilon \text{ sd } (0{\cdot}3903\epsilon t), \tag{5.2a}$$

$$a_2^2 = \epsilon^2 + 125{\cdot}9a_1^2, \tag{5.2b}$$

$$a_3^2 = \tfrac{4}{9}\epsilon^2 - 154{\cdot}8a_1^2. \tag{5.2c}$$

We report results for the three cases $\epsilon = 0{\cdot}025$, $\epsilon = 0{\cdot}05$ and $\epsilon = 0{\cdot}1$. In order to compare our results with the predicted results in (5.2), we compute the amplitudes $\alpha_k = |F_k|$ of the modes F_k with wavenumbers $k = 1, 2, 3$, where

$$F_k = \frac{1}{2\pi}\int_0^{2\pi} y_1(e)\, e^{-ikx_1(e)}\, x_{1e}(e)\, de, \tag{5.3}$$

and $z_1(e) = x_1(e) + iy_1(e)$ is the location of the ocean surface. The integrals were calculated with spectral accuracy by usimg the trapezoidal rule.

We compare our results with those of (5.2) in figure 11 and 12 for $\epsilon = 0{\cdot}025$ and $0{\cdot}05$ respectively. Instead of plotting a_1, the surface elevation that corresponds to the internal ($k = 1$) wave, we have plotted b_1, the amplitude of the elevation of the internal interface. Perturbation theory predicts

$$b_1 = 0{\cdot}4636\epsilon \text{ sd } (0{\cdot}3903\epsilon t). \tag{5.4}$$

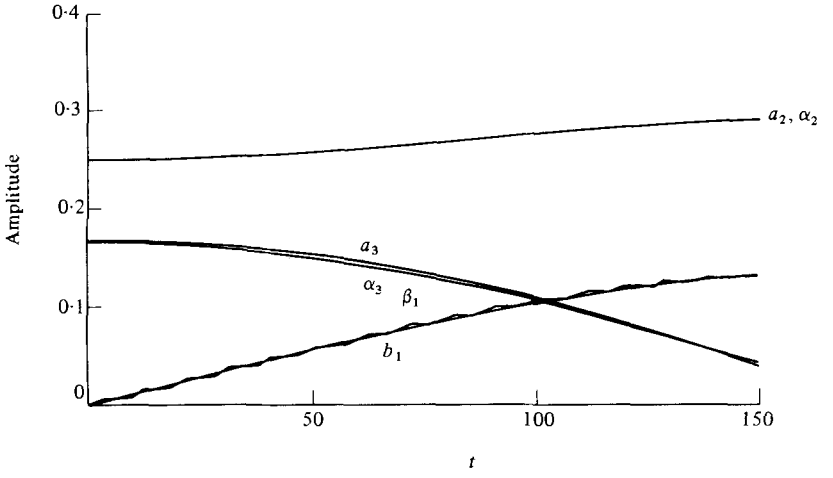

FIGURE 11. The temporal change in the absolute value of the amplitudes of the modes forming a resonant triad; perturbation theory with $\epsilon = 0{\cdot}025$ predicts the curves labelled b_1 (an interfacial wave with $k = 1$), a_2 (a surface wave with $k = 2$) and a_3 (a surface wave with $k = 3$). The fully nonlinear numerical simulations give the curves labelled β_1 (the interfacial wave with $k = 1$), α_2 (the surface wave with $k = 2$), and α_3 (the surface wave with $k = 3$).

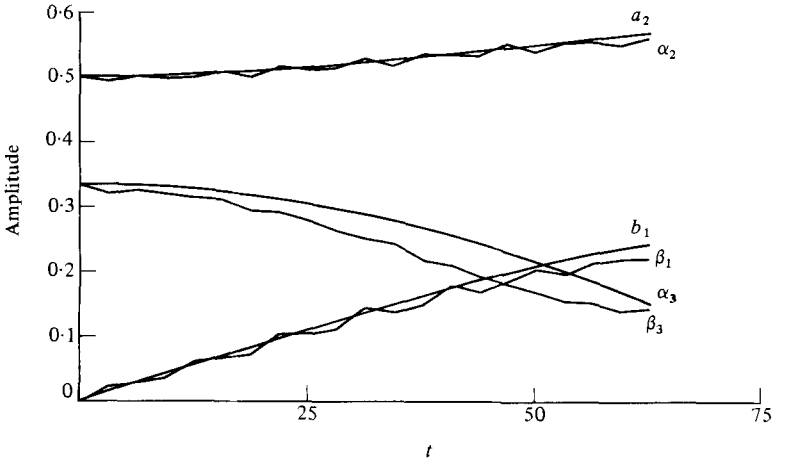

FIGURE 12. Same as figure 11 except $\epsilon = 0{\cdot}05$.

The corresponding nonlinear amplitude with absolute value $\beta_k = |F_k|$ is computed from our results by using the internal interface coordinates $z_2(\varrho) = x_2(\varrho) + iy_2(\varrho)$ in (5.3).

For $\epsilon = 0{\cdot}025$ (figure 11), there is excellent agreement between the perturbation results and the nonlinear results computed by our technique. For the numerical computation, we used 64 points along each interface and a time step of $\frac{1}{100}\pi$. In figure 11 the results are given for $t \leqslant 150$. Shortly thereafter our calculations lose accuracy; energy conservation (variations were less than 0·001 %) deteriorates and small-scale oscillations appear in the interfacial profiles. By increasing the number of points and,

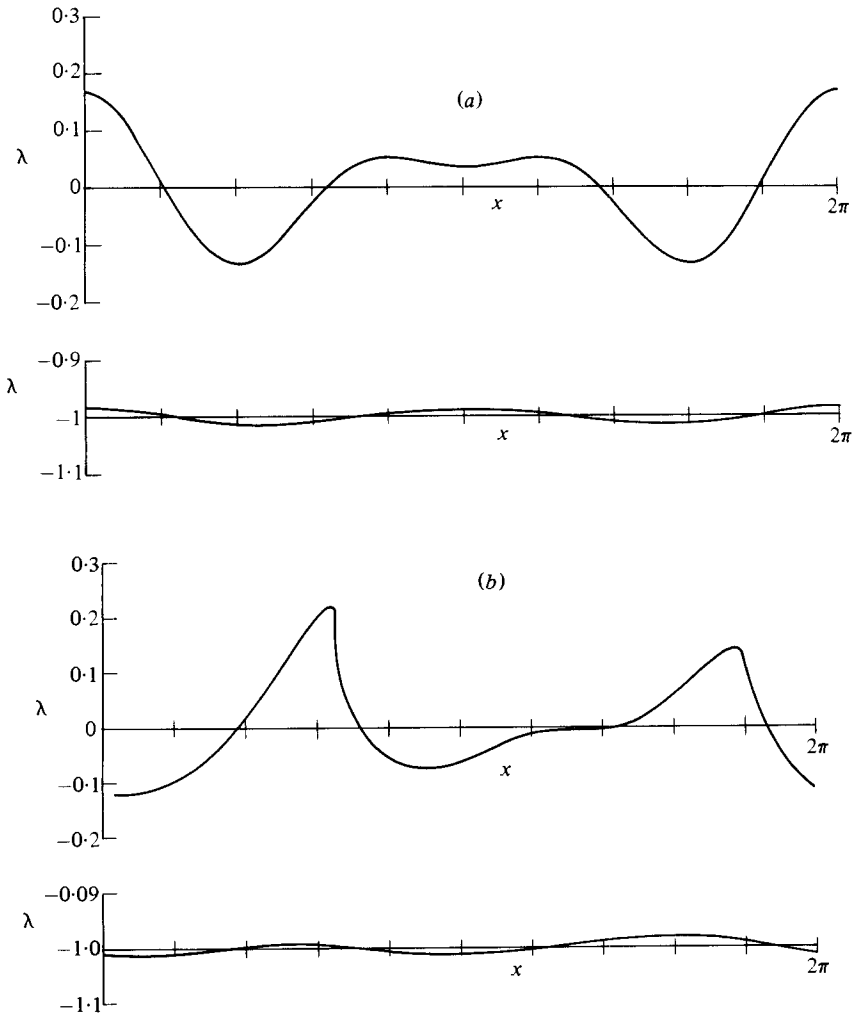

FIGURE 13. (a) Initial profiles of the surface ($y = 0$) and internal interface ($y = -1$). (b) Profiles of the surface ($y = 0$) and internal interface ($y = -1$) at time $t = 2{\cdot}513$.

if necessary, decreasing the time step, the calculations can be extended accurately farther in time but for the present purposes the results were deemed sufficient.

For $\epsilon = 0{\cdot}05$ (figure 12), the accuracy of the perturbation analysis deteriorates. Besides the occurrence of high-frequency modulation of the amplitudes, presumably resulting mainly from $O(\epsilon^2)$ contributions, there is a slight mean deviation between the nonlinear results and the predictions of perturbation theory. In this case, we use 128 points per interface and a time step of $\frac{1}{200}\pi$. The accuracy of our results is confirmed by energy conservation (variations were less than 0·01 %) and by comparison with the results using 64 points per interface and a time step of $\frac{1}{100}\pi$.

For $\epsilon = 0{\cdot}1$, the triad resonance leads directly to the breaking of the ($k = 2$) surface wave. We illustrate this result in figure 13; we show the initial interfacial profiles and later profiles where breaking is about to occur. Obviously the perturbation analysis is not valid in this case. In conclusion we see that our results are consistent with the

estimate of Craik & Adams that accuracy of the perturbation results requires $ak \lesssim 0{\cdot}05$ or $a/\lambda \lesssim 0{\cdot}01$, where λ is the wavelength of the primary mode. It seems that the perturbation theory is only valid for very-small-amplitude waves.

6. Generalizations and other applications

In this paper, equations determining the motion of free surfaces of incompressible, inviscid irrotational flow were obtained as Fredholm integral equations of the second kind. The advantage of such a formulation is that the resulting equations may be solved iteratively by constructing successive terms of a Neumann series. The resulting scheme is globally convergent. Moreover, improved first estimates for the solution at time t can be obtained by standard extrapolation techniques from values at previous time steps. In this way, the solutions are obtained using only a few (2–5) iterations per time step, even for severely deformed geometries.

While the equations given in §2 are specifically for two-dimensional flow, there is a more general formulation, valid in three-dimensional flow. The potential evaluated at the field point r is given by

$$\Phi(r) = \int \mu_{\mathrm{F}}(\mathbf{r}') \frac{\partial}{\partial \nu'} G(\mathbf{r}, \mathbf{r}')\, d\mathbf{r}' + \int \sigma_{\mathrm{B}}(\mathbf{r}') G(\mathbf{r}, \mathbf{r}')\, d\mathbf{r}', \tag{6.1}$$

where $G(\mathbf{r}, \mathbf{r}')$ is the free-space Green function for Laplace's equation, $\partial G/\partial \nu'$ is the normal derivative on the surface, and the integration is over free surfaces for μ_{F} and over solid boundaries for σ_{B}. For two-dimensional flow, $G = (2\pi)^{-1} |\mathbf{r}-\mathbf{r}'|$; for three-dimensional flow, $G = (4\pi)^{-1}/|\mathbf{r}-\mathbf{r}'|$; for axisymmetric flow G can be expressed in terms of elliptic functions of the first kind.

Continuity of normal velocities at free surfaces is automatically satisfied by (6.1), but the requirement that the fluid has no normal velocity relative to solid boundaries leads to Fredholm integral equations of the second kind for μ_{B}. The Neumann series for the solution to these equations, involving any of the Green functions mentioned above, are globally convergent so the equations can be solved iteratively.

This work was supported by the General Hydromechanics Research Program of the Naval Sea Systems Command under ONR Contract N00014-80-C-0129, ONR Contract N00014-77-C-0138, AFOSR Grant no. 77-3405, and the Los Alamos Scientific Laboratory, which is supported by the Department of Energy.

Appendix. Surface and interfacial waves of permanent form

In a stably stratified fluid, (2.6) and (2.14) admit nonlinear travelling-wave solutions of permanent form. For Atwood ratio $A = +1$ ($\rho_2 = 0$) these solutions correspond to the well-known Stokes surface waves. One way to obtain the profiles and nonlinear phase speeds of Stokes waves is to use Padé approximants to sum a computer-extended series in the wave height. This approach was applied by Holyer (1979) in her study of interfacial waves with $0 < A \leqslant 1$.

Many series terms are required for the Padé approximants to converge, and it has been found that methods based on nonlinear integral equations offer increased accuracy at these amplitudes. Several formulations are available for Stokes waves ($A = +1$). For example, Chen & Saffman (1979) use a vortex-sheet representation to derive nonlinear integrodifferential equations for permanent surface waves. For

interfacial waves Vanden-Broek (1980) has recently formulated an integral equation using the steady-state potential coordinate to parametrize the interface.

In this appendix we derive yet another integral equation for interfacial waves. It has the advantage that the steady-state dipole strength is computed directly along with the shape of the interface and nonlinear phase speed. This solution can then be used as an initial condition for (2.6) and (2.14).

We shall restrict ourselves to symmetric wave profiles. The technique may be readily extended to waves of mixed parity using the methods described by Chen & Saffman. The specialization to even profiles allows us to restrict the region of integration to $0 < x < \pi$. Then the interface and dipole strength have the Fourier expansions

$$x(e) = e - \alpha \sin e, \quad y(e) = \sum_{n=1}^{\infty} H_n \cos ne, \quad \mu(e) = \sum_{n=1}^{\infty} M_n \sin ne. \tag{A 1}$$

We choose to work in terms of the dipole-sheet formulation as fewer derivatives with respect to e are required. The x-coordinate of the interface is specified, while the y-coordinates and dipole strength μ are the unknowns. In addition, we must determine the phase speed c of the nonlinear wave.

In the rest frame of the wave the kinematic interface condition $dy/dt = v$ is simply

$$(u-c)\frac{dy}{de} = v\frac{dx}{de}. \tag{A 2}$$

The dynamic interface condition (2.14) becomes

$$(u-c)\frac{\gamma}{x_e} = -2A\left[\tfrac{1}{2}u^2 - cu + \tfrac{1}{2}v^2 + \frac{\gamma^2}{8z_e z_e^*} + y(e) + K\right], \tag{A 3}$$

where we choose $\alpha = 0$ in (2.7), $g = 1$, and

$$\begin{aligned} u(e) - iv(e) = {} & \frac{1}{4\pi i}\int_0^{\pi} \frac{\gamma(e')\, z_e(e) - \gamma(e)\, z_e(e')}{z_e(e)} \cot \tfrac{1}{2}[z(e) - z(e')]\, de' \\ & + \frac{1}{4\pi i}\int_0^{\pi} \frac{\gamma(e')\, z_e(e) - \gamma(e)\, z_e^*(e')}{z_e(e)} \cot \tfrac{1}{2}[z(e) + z^*(e')]\, de'. \end{aligned} \tag{A 4}$$

K is the Bernoulli constant. Note that (A 4) makes explicit use of the symmetries of $y(e)$ and $\mu(e)$. In order to determine $y(e)$ and $\mu(e)$ uniquely we must fix the wave height and mean level of the wave. This is done through the auxiliary conditions

$$\int_0^{2\pi} y(e)\frac{dx}{de}\, de = 0, \quad \tfrac{1}{2}[y(e=0) - y(e=\pi)] = h, \tag{A 5}$$

where h is the specified height.

Evaluating (A 2), (A 3) at the $N+1$ points $e_j = \pi j/N$ $(j = 0, \ldots, N)$, $2N+2$ equations are generated. With the inclusion of the constraints (A 5), there are $2N+4$ equations for $2N+4$ unknowns: y_j, μ_j $(j = 0, \ldots, N)$, c and K. However an examination of the symmetry properties of x, y, u and v reveals that the left- and right-hand sides of (A 2) vanish identically for $e = 0$ and $e = \pi$, reducing the number of equations by two. A corresponding reduction in the number of variables is achieved by noting that both $\mu(e = 0)$ and $\mu(e = \pi)$ must also vanish by symmetry.

In order to solve (A 2), (A 3) it is necessary to relate $\gamma = \mu_e$ and y_e to μ and y

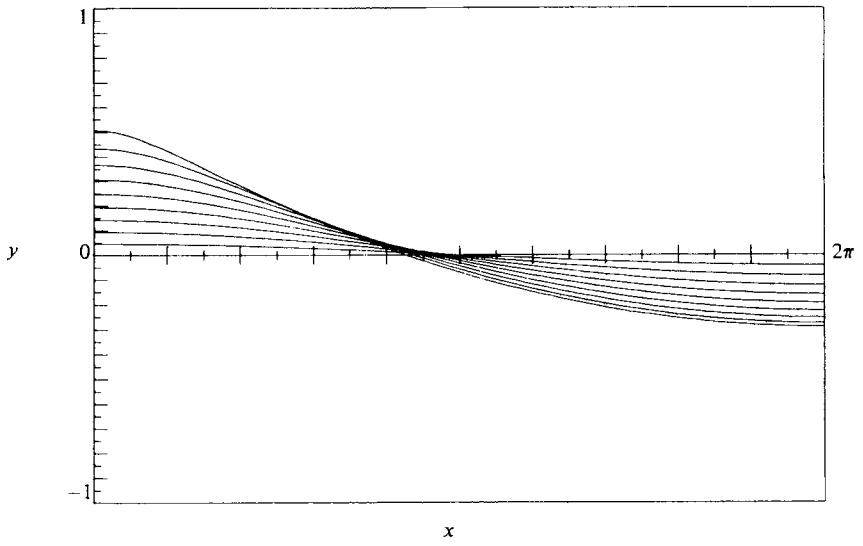

FIGURE 14. A plot of Stokes wave profiles ($A = 1$) at amplitudes $a = 0{\cdot}0(0{\cdot}1)0{\cdot}9a_{\max}$, where $a_{\max} = 0{\cdot}43$.

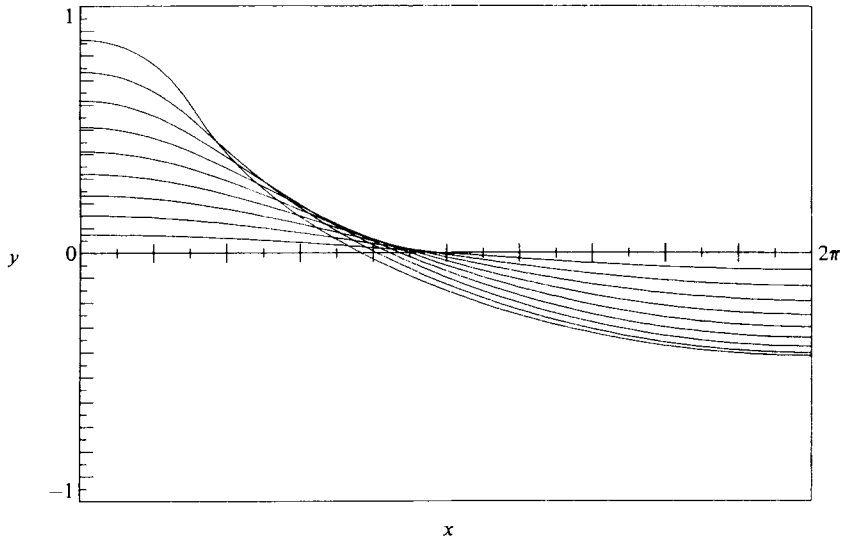

FIGURE 15. A plot of interfacial wave profiles ($A = 0{\cdot}8182$) at amplitudes $a = 0{\cdot}0(0{\cdot}1)0{\cdot}9a_{\max}$, where $a_{\max} = 0{\cdot}71$.

through a differential operator. Vanden-Broek (1980) uses a high-order finite-difference operator. We prefer to use a spectral operator

$$\gamma(i) = \sum_{j=1}^{N} B_{ij}\,\mu(j), \quad y_e(i) = \sum_{j=1}^{N} A_{ij}\,y(j).$$

Here

$$A_{ij} = \frac{2}{N\bar{c}_j}\sum_{k=0}^{N} k\cos\frac{\pi jk}{N}\sin\frac{\pi ik}{N}, \quad B_{ij} = \frac{2}{N\bar{c}_j}\sum_{k=0}^{N} k\sin\frac{\pi jk}{N}\cos\frac{\pi ik}{N},$$

where $\bar{c}_0 = \bar{c}_N = 2$, $\bar{c}_j = 1$ $(0 < j < N)$.

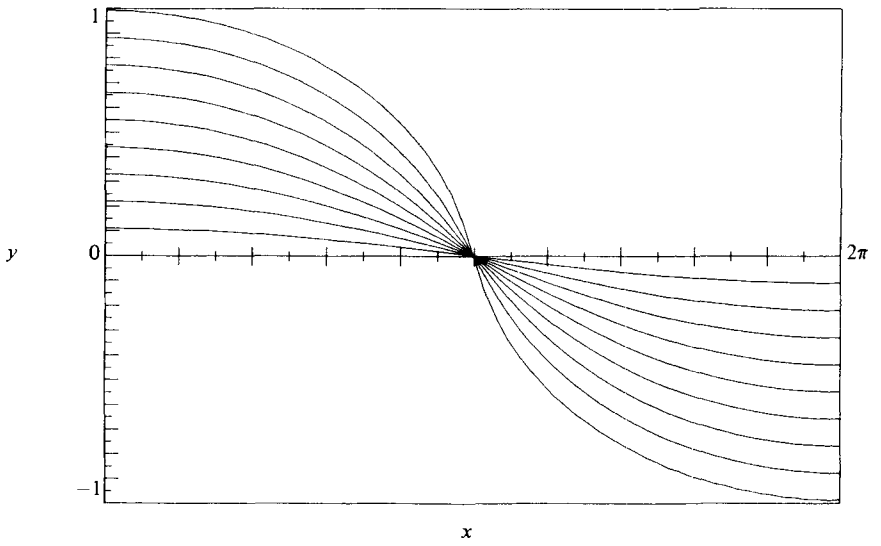

FIGURE 16. A plot of nearly Boussinesq wave profiles ($A = 0{\cdot}005$) at amplitudes $a = 0{\cdot}0(0{\cdot}1)(0{\cdot}0)a_{\max}$, where $a_{\max} = 1{\cdot}1$.

It is crucial that the accuracy of the quadrature scheme used in evaluating the integrals be comparable to the high accuracy afforded by the spectral operators. The most accurate quadrature for this purpose is the trapezoidal rule, but it is important that the limiting values in the integrands as $e \to e'$ be taken into account. With these provisions the equations (A 2)–(A 5) may be solved by Newton's method.

The results for the three Atwood ratios $A = +1$, $A = +0{\cdot}8181$ and $A = +0{\cdot}005$ are shown in figures 14–16 respectively. The Atwood ratio of $+0{\cdot}005$ gives nearly a Boussinesq interfacial wave. For the waves shown in figures 14–16, 65 points were used. It is interesting to note that there is no need to cluster points near the crest as was done by Chen & Saffman in order to obtain convergence. This remained true even for wave amplitudes that were 99% of the maximum. This is due in part to the high accuracy of the spectral derivative.

REFERENCES

BAKER, G. R. 1980 *J. Fluid Mech.* **100**, 209.

BAKER, G. R., MEIRON, D. I. & ORSZAG, S. A. 1980 *Phys. Fluids* **23**, 1485.

BAKER, G. R., MEIRON, D. I. & ORSZAG, S. A. 1982 In preparation.

BALL, F. K. 1964 *J. Fluid Mech.* **19**, 465.

BERGMAN, S. & SCHIFFER, M. 1953 *Kernel Functions and Elliptic Differential Equations in Mathematical Physics*, p. 334. Academic.

CHAN, R. K. & STREET, R. L. 1970 *Tech. Rep. no.* 135, *Dept Civil Engng, Stanford University.*

CHEN, B. & SAFFMAN, P. G. 1979 *Stud. Appl. Math.* **60**, 183.

CRAIK, A. D. D. & ADAM, J. A. 1979 *J. Fluid Mech.* **92**, 15.

HASSELMAN, K. 1966 *Rev. Geophys.* **4**, 801.

HOLYER, J. 1979 *J. Fluid Mech.* **93**, 433.

KELLOGG, O. D. 1953 *Foundations of Potential Theory.* Dover.

KENYON, K. 1966 Ph.D. thesis University of California, San Diego.

LONGUET-HIGGINS, M. S. 1981 *Proc. R. Soc. Lond.* A **376**, 377.

LONGUET-HIGGINS, M. S. & COKELET, E. D. 1976 *Proc. R. Soc. Lond.* A **350**, 1.

PEREGRINE, D. H., COKELET, E. D. & MCIVER, P. 1980 In *Proc. 17th Conf. on Coastal Engng.*

SCHIFFER, M. 1959 *Pacific J. Math.* **9**, 211.

VANDEN-BROEK, J. M. 1980 *Phys. Fluids* **23**, 1723.

VERDON, C. P., MCCRORY, R. L., MORSE, R. L., BAKER, G. R., MEIRON, D. I. & ORSZAG, S. A. 1982 Nonlinear effects of multi-frequency hydrodynamic instabilities on ablatively accelerating thin shells. *Phys. Fluids* (to be published).

VINJE, T. & BREVIG, P. 1981 *Adv. Water Resources* **4**, 77.

WATSON, K. M., WEST, N. J. & COHEN, B. I. 1976 *J. Fluid Mech.* **77**, 185.